A Study of Ionospheric Heavy Ions in the Terrestrial Magnetotail Using ARTEMIS

Mohammad Barani[1], Andrew R. Poppe[1], Matt O. Fillingim[1], J. P. McFadden[1], J. S. Halekas[2]

[1] Space Sciences Laboratory, University of California at Berkeley, California, USA

[2] Dept. of Physics and Astronomy, Univ. Iowa, Iowa City, Iowa, USA

Abstract

Ionospheric heavy ions in the distant tail of the Earth's magnetosphere at lunar distances are observed using the ARTEMIS mission. These heavy ions are originally produced in the terrestrial ionosphere. Using the ElectroStatic Analyzers (ESA) onboard the two probes orbiting the Moon, these heavy ions are observed as cold populations with distinct energies higher than the baseline energy of protons, with the energy-per-charge values for the heavy populations highly correlated with the proton energies. We conducted a full solar cycle survey of these heavy ion observations, including the flux, location, and drift energy, as well as the correlations with the solar wind and geomagnetic indices. The likelihood of finding these heavy ions in the preferred regions of observation called "loaded" quadrants of the terrestrial magnetotail is ~90%, regardless of the z orientation of the IMF. We characterize the ratio of the heavy ion energy to the proton energy, as well as the velocity ratio of these two populations, for events from 2010 to mid-2023. This study shows that the "common velocity" assumption for the proton and heavy ion particles, as suggested in previous work through the velocity filter effect, is not necessarily valid in this case. Challenges in the identification of the mass of the heavy ions due to the ESA's lack of ion composition discrimination are addressed. It is proposed that at the lunar distances the heavy ion population mainly consists of atomic oxygen ions (O^+) with velocities ~25% more than the velocity of the co-located proton population.

1. Introduction

Since the first observations of atomic oxygen (O^+) ions in the Earth's magnetosphere in the early 1970s (Shelley et al., 1972), multiple studies have addressed the source mechanisms, fate, and

distribution of such heavy ions within the magnetosphere (for a historical overview of the role of the Earth's ionosphere in providing plasma to the terrestrial magnetosphere, see (Chappell, 2015)). Heavy ion flux is a good measure for the Earth's ionospheric response in particular and magnetospheric response in general to solar wind activity. The amount of observed heavy ions in the magnetosphere primarily depends on the rate and composition of the outflow from the ionospheric region, their pathways through the magnetosphere, and the mechanisms by which they mix and interact with the solar wind particles and magnetic fields. Extreme UltraViolet (EUV) radiation from the sun, downward electromagnetic energy Poynting flux, and electron precipitation are among the main drivers of the outflowing heavy ions (Cully et al., 2003; Kronberg et al., 2014; Yau, Beckwith, et al., 1985). During solar maxima as well as at summer solstices, the increase in the ionospheric scale heights cause an increase in the O^+-Hydrogen charge-exchange altitude, and therefore enhances the survivability of O^+ (see Figure 9 of (Yau, Beckwith, et al., 1985)). O^+ contributes to the dynamics and physical operation of several magnetospheric phenomena by affecting the tail current sheet thickness and structure, magnetic islands in the magnetotail, reconnection rate, damping rate of the EMIC waves that alters the radiation belt dynamics, and ring current build-up and decay (Kronberg et al., 2014).

Previous observations have established that heavy ions originate primarily from the terrestrial ionospheric regions and can reach the terrestrial magnetotail through several potential pathways (Cladis, 1986; Nilsson et al., 2008; Poppe et al., 2016; K. Seki et al., 1998; Slapak & Nilsson, 2018). An interesting subset of observations are events called Cold Oxygen Beams (COBs) detected in the magnetotail, where "Cold" refers to the narrow thermal energy width of these heavy ion populations (K. Seki et al., 1998). The velocity filter effect is suggested to account for this narrow width. Assuming the conservation of first adiabatic invariant, μ (ratio of perpendicular kinetic energy to the magnetic field strength (Kivelson & Russell, 1995; Roederer, 1970)), and conservation of the ion kinetic energy between the ionosphere and the magnetotail locations, the tail ions gain a smaller pitch angle (higher field-aligned velocity, $v_{\parallel}$) since the magnetic field values close to the ionosphere are larger than the ones at the tail region. Therefore, the ion distribution function at the tail will possess a narrower width in the perpendicular velocity space compared to the distribution function closer to the ionosphere. Additionally, because of the ions' drifts toward the tail region, the distribution function of the tail

populations has to gain cutoffs in $v_{\parallel}$ domain to respond to the convection fields and the width of the source, and there would be a net bulk velocity gain after this transport. This pitch-angle modification (or velocity-dispersed transport) becomes more prominent for the ions that escape the ionosphere with higher temperature-to-velocity ratios (Seki et al., 2000; Kanako Seki et al., 1998). Considering this velocity-filter effect, previous work has suggested that there are different mechanisms that can cause the concurrently streaming populations to drift with the same velocity (see (Nilsson et al., 2008) and references therein). These mechanisms act in a way that the energy gain by the heavier ions per travel distance along the magnetic field lines should be higher than the energy gain by the lighter ions per travel distance such that by the time they reach at the lunar distances in the magnetotail, ions with different masses reach the same velocity regardless of their initial velocity (Nilsson et al., 2008). The drawback is that it predicts all species should end up with a narrow velocity spread at the tail while the observation shows that although the heavier ions gain a narrow width in velocity, the concurrently measured protons do not gain a narrow energy width (K. Seki et al., 1998). However, there is a broader source for protons and as some of the protons supplying the magnetotail do not come from the ionosphere and they do not have the same fate as heavy ions, we would not necessarily expect them to also be narrow in energy width.

Different mechanisms/scenarios have been suggested for the dynamics of these heavy populations as they escape from the polar ionosphere and enter the magnetosphere (Poppe et al., 2016; Seki et al., 2002; K. Seki et al., 1998): (1) The first possible scenario is the direct drift of the dayside polar ionospheric ion outflow from the cusp regions through the velocity-filter mechanism toward the magnetotail; however, (K. Seki et al., 1998) cast doubt on this scenario as the primary mechanism since the average energy of heavy ions measured in the downstream magnetotail by Geotail was ~3.4 keV while other observations have shown that the dominant (90% of measured total ion outflow) heavy ions in the ionospheric outflows through cusp have energies well below 1 keV (Yau, Shelley, et al., 1985). Therefore, the velocity-filter mechanism through this pathway is unlikely to supply sufficient energy and thus, other mechanisms are required to increase heavy ion energies to the measured values. (2) The second possibility is a pathway whereby field-aligned ions are ejected from the nightside ionosphere yet trapped within the near-earth current sheet, then drift toward the dayside magnetopause while magnetically

mirroring within the inner magnetosphere, and then follow the recently reconnected and dragged magnetic field lines to reach the dayside cusp. Via interactions with the cusp, these ions are further energized and convected over the polar caps to finally reach the magnetotail. (3) The third scenario is energization of ionospheric ions that are ejected from the dayside regions of the ionosphere, and then mix with hot sheath ions near the dayside magnetopause before being convected away through dayside reconnection. Interactions with dayside reconnection processes potentially energize these ions further, before they are convected up and over the polar cap regions. This scenario also faces difficulties to be valid. For example, (K. Seki et al., 1998) argued that the plasmaspheric heavy ions that are thought to supply this mechanism are seemingly insufficient to explain the heavy ion beams measured at the tail with energies of more than 1 keV. For a schematic illustration of the three mentioned scenarios, we refer the reader to Figure 6 in (K. Seki et al., 1998). Examining and distinguishing between the second and third scenarios are difficult tasks since multi-spacecraft coverage with proper timing at different locations–from the ionosphere (both nightside and dayside) to the inner magnetosphere back to the dayside cusp then to the magnetotail–would be needed for verification. (4) In the fourth scenario proposed by (Poppe et al., 2016), heavy ionospheric ions trapped within the dipolar region of the outer magnetosphere can either encounter the low-latitude boundary layer (LLBL) or undergo shadowing across the magnetopause (Marcucci et al., 2004; Paschalidis et al., 1994; Sibeck et al., 1987). Once within the LLBL or magnetosheath, these heavy ions are ‘picked up’ by the local flow along the magnetospheric flanks and transported far downstream. Under this last scenario, the ionospheric ions do not necessarily encounter the cusp before traveling to the magnetotail as in the second and third scenarios above.

Here, we perform a statistical study of measurements of cold ion beams in the terrestrial magnetotail as observed by NASA’s Acceleration, Reconnection, Turbulence, and Electrodynamics of the Moon’s Interaction with the Sun (ARTEMIS) mission (Angelopoulos, 2011) in order to further understand their distribution, dynamics, variability, and composition. In Section 2, we briefly describe the selection criteria for ARTEMIS heavy ion events. In Section 3, the statistical study of the observation location, as well as a correlation study with the IMF, solar wind, and geomagnetic activity will be addressed. In Section 4, velocity moments and ratios of the observed heavy ions with respect to the concurrently observed protons will be discussed, and

the challenges in resolving the mass of these heavy ions and the consequences in calculating the velocity of these heavy populations will be addressed and statistically demonstrated. Finally, in Section 5, we discuss our results and conclude.

2. ARTEMIS Data Description and Event Selection

2.1. Example Observation

Figure 1 demonstrates an example observation of a COB observed by the ARTEMIS probes, including both the upstream solar wind and geomagnetic indices (a-g) and ARTEMIS magnetic fields (h-i) and particle measurements (j-o). Figure 1(j-k) are the differential ion energy fluxes from the ARTEMIS ElectroStatic Analyzer (ESA) instruments of both probes in Reduced Fast Survey magnetospheric mode (McFadden et al., 2008). Figure 1(l-o) display the ion density and velocity moments from each probe. The clear narrow upper population above 2 keV in panels 1(j-k) is the heavy ion signature that is the target of this study. The magnetic field during this measurement is B_x-dominated with values in the range of ~ 10 to $\sim 20\ nT$ which is a signature of the northern lobe of the magnetotail. The ions are streaming mainly anti-sunward with speeds between ~ 100 to $\sim 200\ km/s$. The density and velocity moments are corrected for the spacecraft potential which was between $\sim +15$ to $\sim +40\ V$ during this time. As seen in the OMNI data panels, 1(a-g), the dayside magnetosphere was struck by two consecutive shock-like solar wind impacts with maximum dynamic pressures of ~ 9 and $\sim 11\ nPa$, respectively, at approximately 2013-08-20/22 UT and 2013-08-21/14 UT. Accordingly, associated with each shock impact, $SYM-H$ went from +40 to -40 nT and from +20 to -30 nT after encountering the first and second shocks, respectively. This solar wind event is identified as an Interplanetary Coronal Mass Ejection (ICME) at L1 in the Cane-Richardson compilation of ICME events based on ACE measurements (http://www.srl.caltech.edu/ACE/ASC/DATA/level3/icmetable2.htm). During the observation as outlined in the orange box in panels 1(a-g), the y component of the IMF was positive with fluctuations between ~5 and ~8 nT, *AE* was fluctuating between 300 and 850 nT, and the K_p index was ~4.

2.2. Statistical Event Selection

Having described an example COB event above, we then conducted a statistical survey to identify and catalog all similar COB events in the ARTEMIS dataset. As the Moon crosses the magnetotail every month, it spends approximately one fourth to one third of its time inside the magnetotail between the dawn and dusk flanks of the bow shock where the magnetosheath, magnetotail lobes, plasma mantle, and tail current sheet are situated. Using the ESA detectors onboard the two ARTEMIS spacecraft (McFadden et al., 2008) orbiting around the Moon (which is at $\sim 60\ R_e$ radial distance from the Earth), we inspected the differential energy flux during each lunar magnetotail crossing during the time period from January 2011 to August 2023, covering more than a full eleven-year solar cycle (solar cycle 24 that started around December of 2008 and solar cycle 25 that started around December of 2019). In particular, we searched for all events in the terrestrial magnetotail that showed evidence of COBs similar to that shown in Figure 1 and those reported by, e.g., (K. Seki et al., 1998) using Geotail data and (Poppe et al., 2016) using ARTEMIS data. The measured ionospheric-origin heavy ions are registered as narrow populations at energies above the main baseline proton energy (i.e., Figure 1 (j) and (k)) such that these populations more or less tend to maintain a relatively constant energy gap with respect to the main proton population, therefore often following the rising and falling trends of the main proton population. During this period, we documented 86 discrete observations of cold ionospheric ion beams in the ARTEMIS data, although we note that each individual discrete event can vary in length from mere minutes to many hours. Within all collected discrete events, we catalogued 154 sub-intervals taken in the higher data-resolution ("Fast Reduced Survey") mode that include 113,528 data points with 1-spin cadence while the remaining data were taken in the lower data-resolution mode ("Slow Survey"). In Fast Survey, the ARTEMIS/ESA instrument returns two types of measurements: a "Full" packet with 32 energies and 88 angles once every 32 spacecraft spins (1 spin takes ~4 sec) and a "Reduced" packet with 24 energies and 50 angles once every single spacecraft spin. In contrast, during Slow Survey, the ESA returns a Full packet with 32 energy channels and 88 angles only once every 128 spins and a Reduced packet with 32 energies averaged over all angles (i.e., no angular resolution) once every single spin. For large-scale correlation studies in Sections 3.1 and 3.2 below, we use the dataset of all ARTEMIS heavy ion observations (i.e., the 86 observations in both Slow and Fast Survey),

while for the more detailed analysis presented in Section 3.3 and later, we use only the 154 sub-intervals of Fast Survey observations due to the need to compute moments of the distribution, which during Slow Survey are either not available due to the lack of angular resolution (Reduced packets) or too infrequently measured (Full packets).

For each ARTEMIS observation, we also retrieved the upstream solar wind parameters and geomagnetic activity indices via the NASA/OMNI dataset (King & Papitashvili, 2005). The OMNI data were shifted by 40 minutes with respect to the times heavy ions were observed at the tail since it takes approximately this long for ions to reach lunar distances within the downstream magnetotail after the solar wind encounters the sub-solar magnetopause. This choice of time is generally consistent with the times acquired in the work done by (Poppe et al., 2016) using test particle back-tracing in a global MHD simulation model. We experimented with different time shifts between 0 and 60 minutes and found no major change in the results discussed below.

3. Observation locations and correlation with solar wind activity

3.1. Asymmetry in the Location of Observations, Correlation with IMF

Using the position data of the two ARTEMIS spacecraft in Geocentric Solar Ecliptic (GSE) coordinate system, Figure 2 demonstrates the location of the probes during the times that heavy ion events are observed from January 2011 to August of 2023. For ease of visualization, the data depicted in Figure 2 are down sampled to 1-minute cadence. The bow shock depicted as the dotted curved line is from the (Slavin & Holzer, 1981) model and the dashed-dotted curve is the predicted location of the magnetopause from (Fairfield, 1971). A slight concentration of the data points closer to both sides of the tail near the magnetopause is noticeable. The data that occur during periods with an averaged positive z component of the interplanetary magnetic field ($\overline{B_{z_{IMF}}} \geq 0$) are shown as magenta circles while those associated with $\overline{B_{z_{IMF}}} < 0$ are shown as black circles. The IMF values are the OMNI data in GSM' coordinate, identical to the Geocentric Solar Magnetospheric (GSM) coordinate system but corrected for the 4° aberration of the Earth's orbital motion around the Sun similar to (K. Seki et al., 1998). In addition, the temporal averaging in the $\overline{B_{z_{IMF}}}$ for each event (to study the effect of southward versus northward IMF) is performed based on the entire observation time of that specific event. The heavy ions' observation locations and the occurrence rate are insensitive to the orientation of the z-

component of the IMF which is also in agreement with the Cluster measurements (Liao et al., 2010). However, the y component of IMF has a major effect on the location of observation that will be addressed later in this manuscript.

While the observed heavy ion events in the ARTEMIS dataset do not immediately appear to be organized in the GSE coordinate frame, an analysis with respect to geomagnetic coordinates reveals a greater degree of organization, similar to that reported in Seki et al. (1998). First we note that in Figure 2 (b-c), the $z_{GSE} = 0$ line is not necessarily the location of the current sheet, for at least two reasons: One is that the GSM' coordinate system was not used, and the other is that the current sheet is not always a single straight and fixed line over time since it moves and curves in both xy_{GSE} and xz_{GSE} planes depending on the solar wind and geomagnetic conditions (Shang et al., 2020). Therefore, the measured value of B_x at lunar distances within the magnetotail in GSM' coordinates is a better proxy for the location with respect to the plasma sheet. Most of the time, positive B_x is a sign of the northern magnetotail lobe while negative B_x shows that the measurement was taken in the southern magnetotail lobe/mantle. It is known that based on the way IMF reconnects with geomagnetic field lines at the dayside magnetopause, there are preferred paths of field lines to open up, merge, and drift towards the nightside (and thereafter towards the magnetotail) after reconnection and merging with the geomagnetic field. The relaxation direction of the to-be-reconnected kinked field lines are such that for positive (negative) $B_{y\,IMF}$ cases, the reconnected field lines open and drag towards the northern (southern) hemisphere near the dawn side while the dragged field lines of the dusk side occur in the southern (northern) hemisphere (Gosling et al., 1985; Gosling et al., 1990; Hardy et al., 1976; K. Seki et al., 1998). The positive $B_{y\,IMF}$ case is demonstrated schematically in Figure 3(a). This asymmetry is also consistent with the asymmetric intensity of auroral electric field disturbances (Heppner, 1972), the flow channels first observed by (Pinnock et al., 1993) in the dayside cusp region using high frequency radars (Herlingshaw et al., 2020; Pinnock et al., 1993; Provan et al., 1999), as well as heavy ion measurements by the polar-orbiting Cluster mission at the magnetotail (Liao et al., 2010). This asymmetric pattern will bring the ions that are attached (frozen) to their field lines to preferred regions if we look at a yz plane cut of the magnetotail. These expected regions are demonstrated in Figure 3(b).

In Figure 3(c), we plot the distribution of observed COB events with respect to their position along the $y_{GSM'}$ component and the locally measured value of B_x. Additionally, we divide the dataset according to the sign of the average upstream $B_{y\,IMF}$ component during each event. The green circles are associated with the events with positive averaged $B_{y\,IMF}$ during their occurrence, while the blue circles are related to the events with negative averaged $B_{y\,IMF}$. Based on the reconnection relaxation patterns and merging the IMF and geomagnetic fields described above, a majority of the heavy ions that experience $\overline{B_{y}}_{IMF} \geq 0$ should land in either northern dawn or southern dusk sections of the magnetotail (green shaded regions in panel (b)), while for the case of $\overline{B_{y}}_{IMF} < 0$, a majority of these ions should land in either the northern dusk or southern dawn sections of the magnetotail (blue shaded regions in Figure 3(b)). As seen in panel 3(c), we find a very good (~90%) agreement between the observed events in the ARTEMIS dataset and the illustrative cartoon presented in Figure 3(a). This correlation further confirms the results of (K. Seki et al., 1998) and (Liao et al., 2010) that the presence of COB events in the magnetotail are highly controlled by the upstream IMF conditions.

Along the vertical axis of Figure 3(d), the locally measured value of B_x is multiplied by the sign of $B_{y\,IMF}$ consistent with the visualization shown in (K. Seki et al., 1998) so that the yellow-shaded sections always show the loaded quadrants (2 and 4) and unshaded ones are always associated with unloaded quadrants (1 and 3). The observation of (Hardy et al., 1976) shows ~ 80% agreement with the expected loaded quadrant locations of the observed ions at the moon surface (Apollo 12, 14, and 15 landing sites). In this work, as depicted in Figure 3(d), the individual occurrence probabilities of COBs in quadrants 1, 2, 3, and 4 are around 5.21%, 40.98%, 5.64%, and 48.18% respectively. Therefore, our results show more than 89% agreement of COB observations within the loaded (2 and 4) quadrants and less than 11% within the unloaded (1 and 3) quadrants. Figure 3(d) further demonstrates that the accumulation of observations does not depend on the z orientation of the IMF as both magenta and black data points are observed at quadrants 2 and 4. Therefore, contrary to the high correlation with $B_{y\,IMF}$ that causes filling the loaded quadrants demonstrated here (Figure 3(c)), no correlation with $B_{z\,IMF}$ is observed which is also consistent with (Hardy et al., 1976) and (Heppner, 1972) results. Therefore, negative $B_{z\,IMF}$ does not seem to be a required factor in observing heavy ions

although the z orientation of IMF is known to be a factor in the efficiency of magnetic reconnection and the overall Dungey cycle.

3.2. Correlations with Solar Wind and Geomagnetic Indices

In addition to the spatial distribution of observed COBs, we also examine their correlation with upstream solar wind and geomagnetic indices. Specifically, we chose three indices with which to compare: the upstream solar wind pressure, P_{dyn}, the auroral electrojet (*AE*), and the *SYM-H* index. The data set chosen for this correlation study is different from the data set used in the previous figures. In this study, we only chose the events associated with slightly more than a full solar cycle of 11 years from January 2011 to January 2022. In addition, we did not limit ourselves to the heavy ion observations of only Reduced Fast Survey magnetospheric mode but rather used the entire set of COB observations in both Slow and Fast Survey modes (see Section 2 above). The start time of each heavy ion observation was recorded regardless of the energy, angle, and time resolution since the correlation study is not related to the feasibility or quality of the velocity moments calculation. Figure 4 shows the probability distributions of COB observation as a function of P_{dyn}, *AE*, and *SYM-H*. As a baseline for comparison, the occurrence rates (in %) of the three mentioned indices during the entire times the probes were located inside the magnetotail (regardless and irrespective of the heavy ion observation) is recorded and demonstrated as gray dashed lines. For all events, the colored lines are associated with the sum over the index values within varying time intervals before the beginning of each heavy ion observation within the magnetotail as described in the legend of Figure 4(a). For example, the blue line shows the all-events-accumulated occurrence rates of the indices recorded during the time periods of $(-24, 0)$ hours with respect to each event start time. With respect to all three indices, the appearance of heavy ion events in the magnetotail is consistently associated with greater solar wind and geomagnetic activity (higher values for P_{dyn} and *AE*; lower values for *SYM-H*). Furthermore, the most active distributions are seen closest to the beginning of the heavy ion observations (i.e., pink curve, within 12 hours of onset) while the distributions for larger times before each event slowly relax back toward the distribution for all tail crossings. We note that the higher occurrence of *SYM-H* compared to the reference line in Figure 4(c) for the positive values above $+10\ nT$ can be interpreted as the rise of this index during the storm sudden

commencement of CME-type events when the Chapman-Ferraro current is increased along the magnetopause and geomagnetic field intensity strengthens (Akasofu & Chapman, 1961; Wang et al., 2010). To ensure that the histogram curves are all statistically different from one another, we performed a two-sided Kolmogorov-Smirnov test and found the distributions to be significantly different at the $<10^{-8}$ level (Goerg & Kaiser, 2009).

We further examined these distributions by selecting only those observations during highly active periods, corresponding to $P_{dyn} > 4\ nPa$, $AE > 800\ nT$, and within $5\ nT$ of the minima in *SYM-H* indices (shown in Table 1). These are the criteria of interest since reaching each of these is a representation of enhanced solar wind or geomagnetic activity as opposed to geomagnetically quiet times. This association study is summarized in Table 1.

- **Association with P_{dyn}**: Looking at all solar wind dynamic pressure values between January 2011 to January 2022, the average P_{dyn} is $\sim 1.90\ nPa$, and around 94% of the times the P_{dyn} is less than $4\ nPa$ (only 6% with $P_{dyn} > 4\ nPa$) while among all the heavy ion events recorded through this time interval at lunar orbit, 71% of the events are associated with at least one period with $P_{dyn} > 4\ nPa$ within 12 hours before the onset of heavy ion observations. In an additional 9% of the events, the closest time with $P_{dyn} > 4\ nPa$ happens between 12 to 24 hours before the heavy ion observation onset (0 epoch) time. In 1% of the cases, we see periods of $P_{dyn} > 4\ nPa$ only within 6 hours *after* the event start time. 19% of the events either have no associated intervals with $P_{dyn} > 4\ nPa$ periods or the P_{dyn} above $4\ nPa$ happened to be at longer times before the observations (i.e., more than a day before the events).
- **Association with AE**: Between January 2011 to January 2022, the average AE is $\sim 166.2\ nT$ and only less than 2% of the values are above 800 nT while regarding the heavy ions observations, 64% of the total recorded events have at least one period of $AE > 800\ nT$ within 12 hours before the observation of the heavy ions. An additional 4% of the events are associated with $AE > 800\ nT$ within 12 to 24 hours before the event onset times. 8% of the events correspond to values of $AE > 800\ nT$ within 6 hours after the observation. This 8% could be understood by the fact that AE is more closely related to the nightside injection periods in the Dungey cycle (Dungey, 1961), and it is expected

to see a lag time in rise of AE to higher than $800\ nT$ values after a solar wind with $P_{dyn} > 4\ nPa$ has already impacted the dayside magnetosphere. 24% of the events either do not have any associated AE above $800\ nT$ or the $AE > 800\ nT$ happened greater than one day before the heavy ion observation.

- **Association with *SYM-H***: During the entire January 2011-January 2022 time period, the average *SYM-H* is -9.65 nT. Looking at the heavy ion events, 37% of the events have a minimum *SYM-H* within 12 hours before the observations and an additional 20% of the events have minimum *SYM-H* occurring within 12 to 24 hours before the observation. Only 7% of the events correspond to a minimum *SYM-H* within more than one day before the heavy ions are observed. 36% of the events correspond to a minimum *SYM-H* within only 6 hours after the observation. This correlation can be interpreted in two different ways: (1) either evidence that most observations occur at the early phase of the event commencements when the *SYM-H* curve has not yet reached its minimum, but the observation of the heavy ions down the tail had already started, or (2) the probes were not immediately in the proper position to capture the start of the heavy ion events at the tail and the actual start times of observation are earlier.

Taken together, these statistical correlations demonstrate that the presence of COB events in the ARTEMIS dataset at lunar distances are strongly correlated with elevated levels of geomagnetic activity.

3.3. Statistical Study of Heavy Versus Proton Populations

In this Section, we come back to the higher quality (Reduced Fast Survey) heavy ion observations from January 2011 to August 2023 presented in Figures 2 and 3 from both ARTEMIS spacecraft. In particular, we wish to analyze and understand the detailed properties of the heavy ion beams, such as their density, flux, velocity, and energy, in particular with respect to the concurrently observed protons. Figure 5 shows an example of the heavy ion moment calculation from ARTEMIS P2 (THEMIS B) for the same event discussed in Figure 1. The first step in the heavy ion moment calculation is separation of all the data that represent the upper COB population, as visualized in panel (b) in differential energy flux. To do so, we separate the upper population by considering only the data points in the ESA data packets that have

corresponding energy values between the two white dashed lines depicted in Figure 5(b). All data below the lower white dashed line are considered to be the proton (main) population while data above the upper white dashed line are likely background noise. The lower and upper white dashed lines were set manually as constant multiples of the proton drift energy such that the two ion beams were visually separated. After that, we subtracted 1 count from the data packets to reduce the chance of counting the background contamination from cosmic rays and/or high-energy photoelectrons in the ESA measurements. As the flux in the heavy population is relatively low, the heavy ion moment calculation is more sensitive to background contamination, detector response, and the existence of any counts that come from the directions different from the proton direction. Note that the analysis of two example heavy ion observations in (Poppe et al., 2016) and our further analysis here has shown that the heavy ion drift is highly co-aligned with the underlying proton flow. Thus, to increase the signal-to-noise ratios for the heavy ion moment calculation, we further filtered out counts in the heavy population data that came from angles $> 30°$ with respect to the velocity vector of the proton population. This angle cut is chosen based on the visual inspection of the events. In most of the events, the angle between heavy ion and proton populations is less than 20° (note that the ESA anode angle resolution is $22.5°$ for magnetospheric mode (McFadden et al., 2008). For the sake of accuracy and to further avoid the contamination by background noise, throughout this study and for the moment calculations of all events, we only consider the data points at the time intervals during which the corresponding proton flux is above the threshold value of $5 \times 10^5\ 1/(\mathrm{cm}^2.\mathrm{s})$. The black solid and magenta solid lines in Figure 5(b) represent calculated drift energies (derived from the drift velocity) of the proton and heavy ion populations, respectively. The moment calculations take into account spacecraft charging corrections as well as weighting factors to incorporate corrections for efficiency variations in the sensors' angle and energy measurements (McFadden et al., 2008). Spacecraft charging correction is performed using the simultaneous spacecraft potential values measured by the ARTEMIS Electric Field Instrument (EFI) (Bonnell et al., 2008). Figure 5(c) shows the ratio of the two aforementioned magenta and black lines (in panel (b)) to calculate the energy ratio of the heavy versus proton ions. The energy ratios are well above 16 for this event (blue dashed line in panel 5(c)), which would correspond to atomic O^+comoving at a velocity identical to that of the protons, yet generally lower than 28-32 (pink dashed line in panel (c)), which would correspond to molecular ionospheric species (e.g., N_2^+,

NO^+, and O_2^+) also comoving with the protons. The values shown in panels (c) and (d) are the running averaged over the window of 1 minute to better visualize the ratios as well as to be consistent with the OMNI data 1-min resolution in correlation with IMF orientation studies.

3.4. Mass Assumption and Velocity Moments Calculations

From the ESAs on board ARTEMIS, the energy per charge of each incoming ion is measured. Due to the lack of mass discrimination (such as a time-of-flight section), the moment calculation of the heavy population should be performed with care. To calculate the drift velocity of the heavy population, one must assume an ion mass. For these observations, the main two candidates for the heavy ion mass are atomic oxygen ion O^+ with mass 16 times the hydrogen mass, and molecular ions within the range near 32 times the hydrogen mass which are O_2^+, N_2^+, and NO^+ (which we call O_2^+ family throughout the paper). We assume for this work that the observed heavy ions have a mass of 16 amu. The reasons for this choice are the following: 1) **Relative Abundance of O^+**: the energy density ratio of molecular ions (O_2^+ family) to that of O^+ in the magnetospheric region with *L* from 3.5 to 6.6 (where *L* is radial distance from the Earth normalized to the Earth's radius) during active times, is on the order of 1% (Klecker et al., 1986), and this value is comparable or even less in the high-altitude (above $300\ km$) ionospheric regions (Seki et al., 2019). Observations within the magnetotail also show $< 3\%$ mean abundance for molecular ions relative to O^+ abundance (Christon et al., 1994) while O^+ is ~1% of H^+ population within the magnetotail (K. Seki et al., 1998). That gives the energy density ratio of $O_2^+$to that of H^+ to be on the order of 0.01%. ARTEMIS might not even be able to detect that extremely low abundance unless there are some other mechanisms that can increase the abundance of O_2^+ and therefore its observation significantly. 2) **Observation during low geomagnetic activity**: In the regions with *L* of 3.5 to 6.6, no O_2^+ was observed during relatively quiet times with geomagnetic activities of $Dst > -30$ (Seki et al., 2019), while we observed many heavy-ion events that are associated with minimum Dst larger (more positive) than -30 in the magnetotail. Therefore, the observed heavy ions down the tail by ARTEMIS are likely O^+ rather than O_2^+. 3) **Dissociative Recombination Rates**: Assuming even the same source and same level of release for both proton and heavy species at the low-altitude ionosphere, the likelihood of an O^+surviving as it escapes the ionosphere is more than that of O_2^+, due to the

rapid loss of O_2^+ in the ionospheric regions above 300 km through dissociative recombination processes (Kelley, 2015; Mitchell & Guberman, 1989; Schunk & Nagy, 2009).

Considering 16 amu (i.e., O^+) for the mass of the measured heavy ions, we calculated the drift velocity ratios ($V_{Heavy(O^+)}/V_{H^+}$) which are depicted for the chosen event study in Figure 5(d). As the ratio is well above 1.0 (blue dotted-dashed line), the velocity of O^+ seems to be more than 25% higher than the proton velocity. Figure 5(h) is the histogram of energy ratios of heavy versus proton population consistent with panel 5(c). Figure 5(i) is the histogram of the velocity ratios consistent with panel (d). For the sake of accuracy, we did not perform any moving average for the data in Figure 4(h-i). The blue and magenta dashed lines in both (c) and (h) are the expected ratios of heavy-to-proton velocity if the heavy ions are either O^+ and O_2^+, respectively, provided they stream with the same bulk velocity as the proton population as the velocity filter effect suggested (same $v_\parallel$ described in introduction section). No assumption for mass is needed for the ratio calculation of panel (c) and (h) since the energy-per-charge is a direct measurement of ESA. Panel 5(i) shows that, assuming O^+ to be the observed heavy ions, the atomic oxygen population streams with a velocity ~25% faster than the underlying proton population.

The histograms of energy and velocity ratios for all the 154 events (a total of 113,528 data points over both ARTEMIS probes) are depicted in Figure 6. Figure 6(a-b) are the occurrence rates (in %) of the heavy-to-proton energy ratios, and 6(c-d) are the occurrence rates of heavy-to-proton velocity ratios. In the velocity ratio panels, O^+ is assumed as the heavy population based on the reasoning discussed earlier in this section. Based on the statistical study for all events, the energy ratio of the heavy populations versus their concurrent proton population on average is ~24 (black dashed lines in Figure 6(a) and (b)). The mean value is also very close to the mode of the distribution, while the median values (black dotted lines) are slightly larger than the modes and means, due to the skewness of the occurrence distributions for higher values than the lower ones. Again, no moving averaging or down sampling was performed for these data as well. Figure 6(c) and (d) shows the most probable velocity ratio to be ~1.25; in other words, heavy ion events of O^+ are typically ~25% faster than protons.

Similarly, Figure 7 demonstrates the flux ratios (panels (a) and (b)) and density ratios (panels (c) and (d)) histograms from ARTEMIS P1 (top panels) and P2 (bottom panels) measurements. The figure shows that the flux and density of heavy ions (J_{Heavy^+} and n_{Heavy^+}) vary within the ranges of $\sim 10^{-4}$ to $\sim 10^{-1}$ times the flux and density (J_{H^+} and n_{H^+}) of the concurrently observed proton populations. The most probable flux and density for heavy ions through our statistical study are:

$$J_{Heavy^+} \approx 2 \times 10^{-3} \, . \, J_{H^+}$$

$$n_{Heavy^+} \approx 1.6 \times 10^{-3} \, . \, n_{H^+}$$

Note that when calculating the heavy ion fluxes, no assumption is needed since flux is among the direct outcomes of the ESA detectors while for density, we assume a mass of 16 amu for the heavy ions since density is not a directly measurable quantity from ESA detectors.

4. Discussion and Conclusion

As discussed in the introduction, Seki et al. (1998) has outlined multiple potential pathways for ionospheric ions to migrate through the magnetosphere and eventually find their way into the deep magnetotail as COBs. Briefly, these include (i) direct O^+ outflow from the polar region with acceleration/energization occurring along the way before injection into the magnetotail lobes and mantle; (ii) nightside outflowing O^+ ions that become equatorially trapped, circulated around to the dayside, injected into the magnetosheath, and finally drug up and over the polar cap region before entering the tail; and, (iii) dayside outflowing O^+ ions that become trapped in the inner equatorial regions, are injected into the magnetosheath, and follow a similar path up and over the polar cap region as in scenario (ii) (see also Figure 6 of (K. Seki et al., 1998)). The Cluster mission has also observed direct escape of O^+ at higher latitudes along newly reconnected magnetosheath field lines (e.g., (Slapak et al., 2012)).

The COB observations by ARTEMIS presented here are analogous to–and indeed, likely of the same nature as–those observed by Geotail over a wider range of downtail distances (e.g., (Seki et al., 2000; K. Seki et al., 1998; Kanako Seki et al., 1998)). In an earlier case-study analysis of these ARTEMIS COB events, however, (Poppe et al., 2016) used combined MHD and test-

particle tracing to show that ions composing the COBs escaped the inner magnetosphere via interactions with the low-latitude boundary layer (LLBL) and/or magnetopause (via magnetopause shadowing) followed by pick up and acceleration in the LLBL/magnetosheath flow without the need to convect over the polar regions and gain further acceleration in the cusp region. This pathway is different from scenarios (ii) and (iii) above in that O^+ ions are considered to escape the inner magnetosphere over a broad range of the dayside LLBL/magnetopause and not just in locations that would cause them to interact with the cusp region.

What is missing at the current stage is a more comprehensive modeling investigation of the efficiency of O^+ interactions with the LLBL and/or magnetopause and subsequent downtail transport as a function of location (i.e., local time and magnetic latitude), initial O^+ energy, pitch angle, L-shell, and geomagnetic activity to complement the limited case study analysis presented in (Poppe et al., 2016). Such a modeling study could also shed light on the observed velocity characteristics of the COBs observed by ARTEMIS. As shown in Figure 6, the origin of the offset and relatively narrow range of observed COB speeds relative to the underlying proton speed ($V_{O^+} \approx 1.25\, V_{H^+}$) remains to be fully elucidated. We note that the example test-particle tracing results in (Poppe et al., 2016) showed that a wide range of initial heavy ion energies (~1 to ~100 keV) and equatorial pitch angles within the quasi-trapped outer magnetosphere could in fact be narrowly focused into identical-energy COBs at lunar distances (see their Figure 4; also note that (Poppe et al., 2016) simulated mass 32 heavy ions as opposed to mass 16–see discussion below). We suggest that this process may be a combination of a velocity-filter effect, which acts to disperse the ions in location according to their velocity, and a centrifugal acceleration effect, which acts to increase the parallel velocity of the ions (e.g., (Cladis, 1986)). In particular, the centrifugal acceleration of polar-cap field lines has been shown to accelerate polar ionospheric ions to velocities an order-of-magnitude higher than their initial velocity as magnetic field lines are convected over the polar cap. For our purposes, a lesser centrifugal acceleration would be required (only an excess of ~25%) as field lines–and the frozen-in O^+ ions attached to such field lines–are convected along the flanks of the magnetopause downtail. Alternatively, interaction of O^+ ions with the LLBL, which has been observed to maintain velocities larger than the adjacent magnetosheath (e.g., (Gosling et al., 1990; Sonnerup et al.,

1981)) could pre-accelerate the O^+ ions to velocities above the LLBL protons before they convect further down the flanks. Nevertheless, a more in-depth and rigorous test-particle tracing study is likely needed to further elucidate and test these hypotheses.

We note the difference between the density ratio of O^+ to that of H^+ in this work compared to the work done by (K. Seki et al., 1998). As mentioned, the average density ratio observed with ARTEMIS is ~0.16%, while Geotail observations (K. Seki et al., 1998) reported this ratio to be one order of magnitude larger (between ~1% to ~3% at lunar distances). Previously (K. Seki et al., 1998) argued that as their observed percentage of the COB density with respect to H^+density in magnetotail is more than the typical plasmaspheric ~0.1% values (Olsen et al., 1987), the plasmaspheric O^+ cannot be the supplier of the magnetotail COBs. Here, our lower reported percentage values for this ratio would not necessarily rule out the possibility of the plasmaspheric O^+ to be a source for the observed COBs measured downtail by ARTEMIS.

We also note that prior to this study, (Poppe et al., 2016) presented ARTEMIS observations of cold ion beams in the terrestrial magnetotail near lunar orbit that they interpreted as ionospheric molecular ions (i.e., some combination of N_2^+, NO^+, and O_2^+) based on the drift energy of these cold beams relative to the underlying drift energy of concurrently observed magnetosheath/boundary layer protons. The drift energy of the cold ion beams analyzed in (Poppe et al., 2016) were closer to values of ~28 than ~16, suggesting molecular species at the same velocity as the underlying protons. Subsequently, however, an independent analysis of similar events observed by Geotail were confirmed to be atomic O^+ and not molecular ions, with the atomic O^+ drifting at a faster speed than the underlying protons (Seki, priv. comm., 2018). This finding is similar to that found here, where under the assumption of O^+ composition, the COB events are found to be at approximately 1.25 times the underlying proton speed. Thus, the events discussed in (Poppe et al., 2016) are more likely to be atomic O^+ moving faster than the underlying protons as opposed to perfectly comoving molecular ions. As the ARTEMIS ESAs lack ion composition discrimination, a definitive identification of the events as either O^+ or O_2^+ might not be possible in this work. A conjunction study with the missions that possess ion mass discrimination would be a future target of study to not only clarify the composition of the COBs but also help to determine the scenario under which the COBs travel from the ionosphere to the magnetotail.

In summary, observation of the heavy ions at the Earth's magnetotail near the lunar orbit shows clear preferred locations of observations known as loaded quadrants in a y-z cross section of magnetotail with a strong correlation (~90%) with the y component of IMF resembling the expected relaxation patterns of the magnetic fields at the Earth's magnetopause after IMF reconnection with geomagnetic field lines. The presence of COB events in the ARTEMIS dataset at lunar distances is strongly correlated with elevated levels of geomagnetic activity. Correlation studies with solar wind and geomagnetic indices of P_{dyn}, *AE,* and *SYM-H* show that the appearance of heavy ion events in the magnetotail is consistently associated with greater solar wind and geomagnetic activities (higher values for P_{dyn} and *AE*; lower values for *SYM-H*). Furthermore, the highest geomagnetic activity is seen temporally closest to the beginning of the heavy ion observations. The reasons for choosing mass of 16 amu was discussed, and it was shown that these O^+ ions stream ~25% faster than the concurrently measured protons. The calculated flux and energy ratios of O^+ with respect to those of the proton populations show that the flux and density of O^+ is ~0.2% and ~0.16% that of the concurrently observed protons. In comparison, these values are approximately one order of magnitude smaller than the reported values from (K. Seki et al., 1998). Based on these observations, we discuss a LLBL and/or magnetopause shadowing scenario following (Poppe et al., 2016) on the fate and pathways of the heavy ions from ionosphere to the tail.

Acknowledgements

The authors gratefully acknowledge support from NASA's Heliophysics Guest Investigator Program, grant #80NSSC20K0691. We acknowledge NASA contract NAS5-02099 and V. Angelopoulos for use of data from the THEMIS Mission. Specifically, we thank J. W. Bonnell and F. S. Mozer for use of EFI data, and K. H. Glassmeier, U. Auster and W. Baumjohann for the use of FGM data provided under the lead of the Technical University of Braunschweig and with financial support through the German Ministry for Economy and Technology and the German Center for Aviation and Space (DLR) under contract 50 OC 0302. M. Barani thanks Shaosui Xu for the useful discussion and coding advice. M. Barani also thanks John W. Bonnell

and David G. Sibeck for the science discussions, and Mary K. Hudson for reading the manuscript and for the suggestions.

References

Akasofu, S. I., & Chapman, S. (1961). The ring current, geomagnetic disturbance, and the Van Allen radiation belts. *Journal of Geophysical Research (1896-1977)*, *66*(5), 1321-1350. https://doi.org/https://doi.org/10.1029/JZ066i005p01321

Angelopoulos, V. (2011). The ARTEMIS Mission. *Space Science Reviews*, *165*(1), 3-25. https://doi.org/10.1007/s11214-010-9687-2

Bonnell, J. W., Mozer, F. S., Delory, G. T., Hull, A. J., Ergun, R. E., Cully, C. M., . . . Harvey, P. R. (2008). The Electric Field Instrument (EFI) for THEMIS. *Space Science Reviews*, *141*(1), 303-341. https://doi.org/10.1007/s11214-008-9469-2

Chappell, C. R. (2015). The Role of the Ionosphere in Providing Plasma to the Terrestrial Magnetosphere—An Historical Overview. *Space Science Reviews*, *192*(1), 5-25. https://doi.org/10.1007/s11214-015-0168-5

Christon, S. P., Gloeckler, G., Williams, D. J., Mukai, T., McEntire, R. W., Jacquey, C., . . . Yamamoto, T. (1994). Energetic atomic and molecular ions of ionospheric origin observed in distant magnetotail flow-reversal events. *Geophysical Research Letters*, *21*(25), 3023-3026. https://doi.org/https://doi.org/10.1029/94GL02095

Cladis, J. B. (1986). Parallel acceleration and transport of ions from polar ionosphere to plasma sheet. *Geophysical Research Letters*, *13*(9), 893-896. https://doi.org/https://doi.org/10.1029/GL013i009p00893

Cully, C. M., Donovan, E. F., Yau, A. W., & Arkos, G. G. (2003). Akebono/Suprathermal Mass Spectrometer observations of low-energy ion outflow: Dependence on magnetic activity and solar wind conditions. *Journal of Geophysical Research: Space Physics*, *108*(A2). https://doi.org/https://doi.org/10.1029/2001JA009200

Dungey, J. W. (1961). Interplanetary Magnetic Field and the Auroral Zones. *Physical Review Letters*, *6*(2), 47-48. https://doi.org/10.1103/PhysRevLett.6.47

Fairfield, D. H. (1971). Average and unusual locations of the Earth's magnetopause and bow shock. *Journal of Geophysical Research (1896-1977)*, *76*(28), 6700-6716. https://doi.org/https://doi.org/10.1029/JA076i028p06700

Goerg, S. J., & Kaiser, J. (2009). Nonparametric testing of distributions—the Epps-Singleton two-sample test using the empirical characteristic function. *Stata Journal*, *9*(3), 454-465.

Gosling, J. T., Baker, D. N., Bame, S. J., Feldman, W. C., Zwickl, R. D., & Smith, E. J. (1985). North-south and dawn-dusk plasma asymmetries in the distant tail lobes: ISEE 3. *Journal of Geophysical Research: Space Physics*, *90*(A7), 6354-6360. https://doi.org/https://doi.org/10.1029/JA090iA07p06354

Gosling, J. T., Thomsen, M. F., Bame, S. J., Elphic, R. C., & Russell, C. T. (1990). Plasma flow reversals at the dayside magnetopause and the origin of asymmetric polar cap convection. *Journal of Geophysical Research: Space Physics*, *95*(A6), 8073-8084. https://doi.org/https://doi.org/10.1029/JA095iA06p08073

Hardy, D. A., Freeman, J. W., & Hills, H. K. (1976, 1976//). Plasma Observations in the Magnetotail. Magnetospheric Particles and Fields, Dordrecht.

Heppner, J. P. (1972). Polar-cap electric field distributions related to the interplanetary magnetic field direction. *Journal of Geophysical Research (1896-1977)*, *77*(25), 4877-4887. https://doi.org/https://doi.org/10.1029/JA077i025p04877

Herlingshaw, K., Baddeley, L. J., Oksavik, K., & Lorentzen, D. A. (2020). A Statistical Study of Polar Cap Flow Channels and Their IMF By Dependence. *Journal of Geophysical Research: Space Physics*, *125*(11), e2020JA028359. https://doi.org/https://doi.org/10.1029/2020JA028359

Kelley, M. C. (2015). MESOSPHERE | Ionosphere. In G. R. North, J. Pyle, & F. Zhang (Eds.), *Encyclopedia of Atmospheric Sciences (Second Edition)* (pp. 422-429). Academic Press. https://doi.org/https://doi.org/10.1016/B978-0-12-382225-3.00184-5

King, J. H., & Papitashvili, N. E. (2005). Solar wind spatial scales in and comparisons of hourly Wind and ACE plasma and magnetic field data. *Journal of Geophysical Research: Space Physics*, *110*(A2). https://doi.org/https://doi.org/10.1029/2004JA010649

Kivelson, M. G., & Russell, C. T. (1995). *Introduction to Space Physics*.

Klecker, B., Möbius, E., Hovestadt, D., Scholer, M., Gloeckler, G., & Ipavich, F. M. (1986). Discovery of energetic molecular ions (NO+ and O2+) in the storm time ring current. *Geophysical Research Letters*, *13*(7), 632-635. https://doi.org/https://doi.org/10.1029/GL013i007p00632

Kronberg, E. A., Ashour-Abdalla, M., Dandouras, I., Delcourt, D. C., Grigorenko, E. E., Kistler, L. M., . . . Zelenyi, L. M. (2014). Circulation of Heavy Ions and Their Dynamical Effects in the Magnetosphere: Recent Observations and Models. *Space Science Reviews*, *184*(1), 173-235. https://doi.org/10.1007/s11214-014-0104-0

Liao, J., Kistler, L. M., Mouikis, C. G., Klecker, B., Dandouras, I., & Zhang, J. C. (2010). Statistical study of O+ transport from the cusp to the lobes with Cluster CODIF data. *Journal of Geophysical Research: Space Physics*, *115*(A12). https://doi.org/https://doi.org/10.1029/2010JA015613

Marcucci, M. F., Bavassano Cattaneo, M. B., Pallocchia, G., Amata, E., Bruno, R., Di Lellis, A. M., . . . Balogh, A. (2004). Energetic magnetospheric oxygen in the magnetosheath and its response to IMF orientation: Cluster observations. *Journal of Geophysical Research: Space Physics*, *109*(A7). https://doi.org/https://doi.org/10.1029/2003JA010312

McFadden, J. P., Carlson, C. W., Larson, D., Ludlam, M., Abiad, R., Elliott, B., . . . Angelopoulos, V. (2008). The THEMIS ESA Plasma Instrument and In-flight Calibration. *Space Science Reviews*, *141*(1), 277-302. https://doi.org/10.1007/s11214-008-9440-2

Mitchell, J. B. A., & Guberman, S. L. (1989). *Dissociative Recombination: Theory, Experiment and Applications* [doi:10.1142/0621]. WORLD SCIENTIFIC. https://doi.org/doi:10.1142/0621

Nilsson, H., Waara, M., Marghitu, O., Yamauchi, M., Lundin, R., Rème, H., . . . Korth, A. (2008). An assessment of the role of the centrifugal acceleration mechanism in high altitude polar cap oxygen ion outflow. *Ann. Geophys.*, *26*(1), 145-157. https://doi.org/10.5194/angeo-26-145-2008

Olsen, R. C., Shawhan, S. D., Gallagher, D. L., Green, J. L., Chappell, C. R., & Anderson, R. R. (1987). Plasma observations at the Earth's magnetic equator. *Journal of Geophysical Research: Space Physics*, *92*(A3), 2385-2407. https://doi.org/https://doi.org/10.1029/JA092iA03p02385

Paschalidis, N. P., Sarris, E. T., Krimigis, S. M., McEntire, R. W., Levine, M. D., Daglis, I. A., & Anagnostopoulos, G. C. (1994). Energetic ion distributions on both sides of the Earth's magnetopause. *Journal of Geophysical Research: Space Physics*, *99*(A5), 8687-8703. https://doi.org/https://doi.org/10.1029/93JA03563

Pinnock, M., Rodger, A. S., Dudeney, J. R., Baker, K. B., Newell, P. T., Greenwald, R. A., & Greenspan, M. E. (1993). Observations of an enhanced convection channel in the cusp ionosphere. *Journal of Geophysical Research: Space Physics*, *98*(A3), 3767-3776. https://doi.org/https://doi.org/10.1029/92JA01382

Poppe, A. R., Fillingim, M. O., Halekas, J. S., Raeder, J., & Angelopoulos, V. (2016). ARTEMIS observations of terrestrial ionospheric molecular ion outflow at the Moon. *Geophysical Research Letters*, *43*(13), 6749-6758. https://doi.org/https://doi.org/10.1002/2016GL069715

Provan, G., Yeoman, T. K., & Cowley, S. W. H. (1999). The influence of the IMF By component on the location of pulsed flows in the dayside ionosphere observed by an HF

radar. *Geophysical Research Letters*, *26*(4), 521-524. https://doi.org/https://doi.org/10.1029/1999GL900009

Roederer, J. G. a. (1970). Dynamics of geomagnetically trapped radiation. *Dynamics of geomagnetically trapped radiation /*.

Schunk, R., & Nagy, A. (2009). *Ionospheres: Physics, Plasma Physics, and Chemistry* (2 ed.). Cambridge University Press. https://doi.org/DOI: 10.1017/CBO9780511635342

Seki, K., Elphic, R. C., Thomsen, M. F., Bonnell, J., Lund, E. J., Hirahara, M., . . . Mukai, T. (2000). Cold flowing O+ beams in the lobe/mantle at Geotail: Does FAST observe the source? *Journal of Geophysical Research: Space Physics*, *105*(A7), 15931-15944. https://doi.org/https://doi.org/10.1029/1999JA900470

Seki, K., Elphic, R. C., Thomsen, M. F., Bonnell, J., McFadden, J. P., Lund, E. J., . . . Mukai, T. (2002). A new perspective on plasma supply mechanisms to the magnetotail from a statistical comparison of dayside mirroring O+ at low altitudes with lobe/mantle beams. *Journal of Geophysical Research: Space Physics*, *107*(A4), SMP 7-1-SMP 7-12. https://doi.org/https://doi.org/10.1029/2001JA900122

Seki, K., Hirahara, M., Terasawa, T., Mukai, T., Saito, Y., Machida, S., . . . Kokubun, S. (1998). Statistical properties and possible supply mechanisms of tailward cold O+ beams in the lobe/mantle regions. *Journal of Geophysical Research: Space Physics*, *103*(A3), 4477-4489. https://doi.org/https://doi.org/10.1029/97JA02137

Seki, K., Keika, K., Kasahara, S., Yokota, S., Hori, T., Asamura, K., . . . Shinohara, I. (2019). Statistical Properties of Molecular Ions in the Ring Current Observed by the Arase (ERG) Satellite. *Geophysical Research Letters*, *46*(15), 8643-8651. https://doi.org/https://doi.org/10.1029/2019GL084163

Seki, K., Terasawa, T., Hirahara, M., & Mukai, T. (1998). Quantification of tailward cold O+ beams in the lobe/mantle regions with Geotail data: Constraints on polar O+ outflows. *Journal of Geophysical Research: Space Physics*, *103*(A12), 29371-29381. https://doi.org/https://doi.org/10.1029/98JA02463

Shang, W. S., Tang, B. B., Shi, Q. Q., Tian, A. M., Zhou, X. Y., Yao, Z. H., . . . Wang, M. (2020). Unusual Location of the Geotail Magnetopause Near Lunar Orbit: A Case Study. *Journal of Geophysical Research: Space Physics*, *125*(4), e2019JA027401. https://doi.org/https://doi.org/10.1029/2019JA027401

Shelley, E. G., Johnson, R. G., & Sharp, R. D. (1972). Satellite observations of energetic heavy ions during a geomagnetic storm. *Journal of Geophysical Research (1896-1977)*, *77*(31), 6104-6110. https://doi.org/https://doi.org/10.1029/JA077i031p06104

Sibeck, D. G., McEntire, R. W., Lui, A. T. Y., Lopez, R. E., Krimigis, S. M., Decker, R. B., . . . Potemra, T. A. (1987). Energetic magnetospheric ions at the dayside magnetopause:

Leakage or merging? *Journal of Geophysical Research: Space Physics*, *92*(A11), 12097-12114. https://doi.org/https://doi.org/10.1029/JA092iA11p12097

Slapak, R., & Nilsson, H. (2018). The Oxygen Ion Circulation in The Outer Terrestrial Magnetosphere and Its Dependence on Geomagnetic Activity. *Geophysical Research Letters*, *45*(23), 12,669-612,676. https://doi.org/https://doi.org/10.1029/2018GL079816

Slapak, R., Nilsson, H., Westerberg, L. G., & Eriksson, A. (2012). Observations of oxygen ions in the dayside magnetosheath associated with southward IMF. *Journal of Geophysical Research: Space Physics*, *117*(A7). https://doi.org/https://doi.org/10.1029/2012JA017754

Slavin, J. A., & Holzer, R. E. (1981). Solar wind flow about the terrestrial planets 1. Modeling bow shock position and shape. *Journal of Geophysical Research: Space Physics*, *86*(A13), 11401-11418. https://doi.org/https://doi.org/10.1029/JA086iA13p11401

Sonnerup, B. U. Ö., Paschmann, G., Papamastorakis, I., Sckopke, N., Haerendel, G., Bame, S. J., . . . Russell, C. T. (1981). Evidence for magnetic field reconnection at the Earth's magnetopause. *Journal of Geophysical Research: Space Physics*, *86*(A12), 10049-10067. https://doi.org/https://doi.org/10.1029/JA086iA12p10049

Wang, C., Li, H., Richardson, J. D., & Kan, J. R. (2010). Interplanetary shock characteristics and associated geosynchronous magnetic field variations estimated from sudden impulses observed on the ground. *Journal of Geophysical Research: Space Physics*, *115*(A9). https://doi.org/https://doi.org/10.1029/2009JA014833

Yau, A. W., Beckwith, P. H., Peterson, W. K., & Shelley, E. G. (1985). Long-term (solar cycle) and seasonal variations of upflowing ionospheric ion events at DE 1 altitudes. *Journal of Geophysical Research: Space Physics*, *90*(A7), 6395-6407. https://doi.org/https://doi.org/10.1029/JA090iA07p06395

Yau, A. W., Shelley, E. G., Peterson, W. K., & Lenchyshyn, L. (1985). Energetic auroral and polar ion outflow at DE 1 altitudes: Magnitude, composition, magnetic activity dependence, and long‐term variations. *Journal of Geophysical Research: Space Physics*, *90*(A9), 8417-8432.

Figure 1.

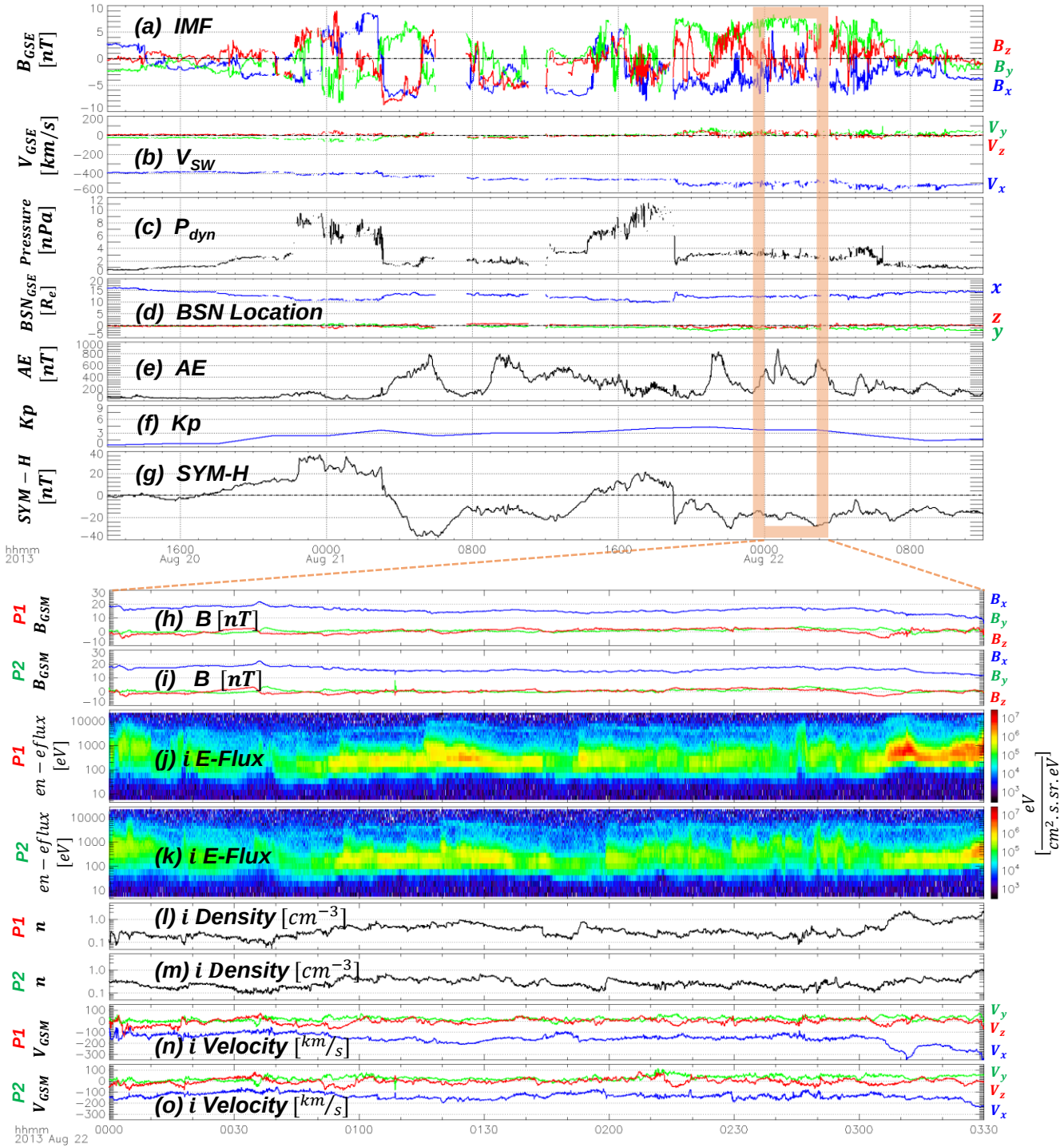

Figure 1. Solar wind and geomagnetic indices (OMNI data, panels (a) to (g)) as well as ARTEMIS P1 and ARTEMIS P2 magnetic field and ions particle data and the corresponding moments during a cold heavy ion measurement on 22 August 2013 between 00:00 and 03:30 UT. Panels (j) and (k) are differential energy flux from ElectroStatic Analyzers in which the cold heavy ion beams are noticeable as upper narrow population situated above the main proton population. Panels (l) and (m) are the ion densities, and (n) and (o) are the drift (bulk) velocity moments.

Figure 2.

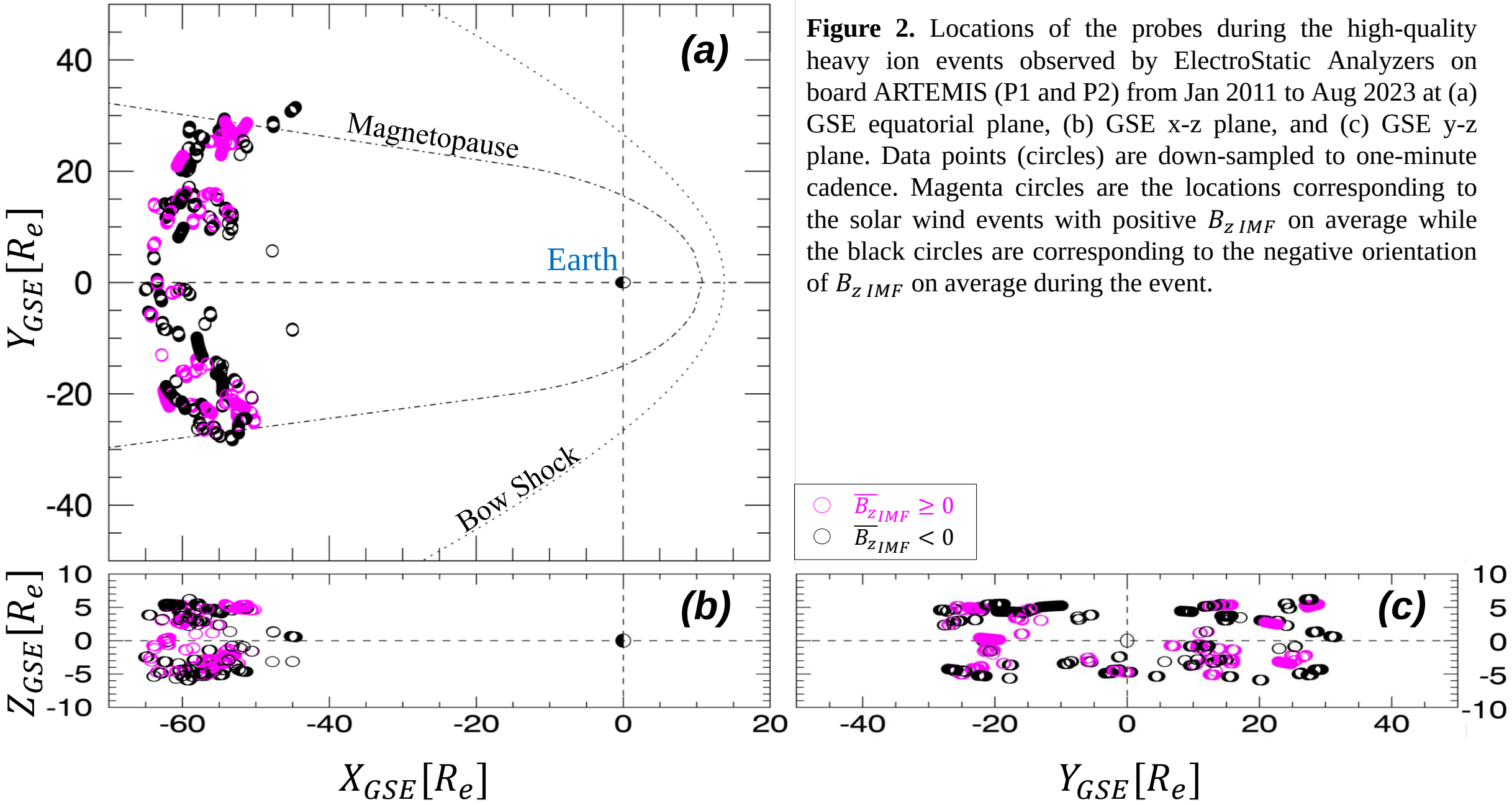

Figure 2. Locations of the probes during the high-quality heavy ion events observed by ElectroStatic Analyzers on board ARTEMIS (P1 and P2) from Jan 2011 to Aug 2023 at (a) GSE equatorial plane, (b) GSE x-z plane, and (c) GSE y-z plane. Data points (circles) are down-sampled to one-minute cadence. Magenta circles are the locations corresponding to the solar wind events with positive $B_{z\,IMF}$ on average while the black circles are corresponding to the negative orientation of $B_{z\,IMF}$ on average during the event.

Figure 3.

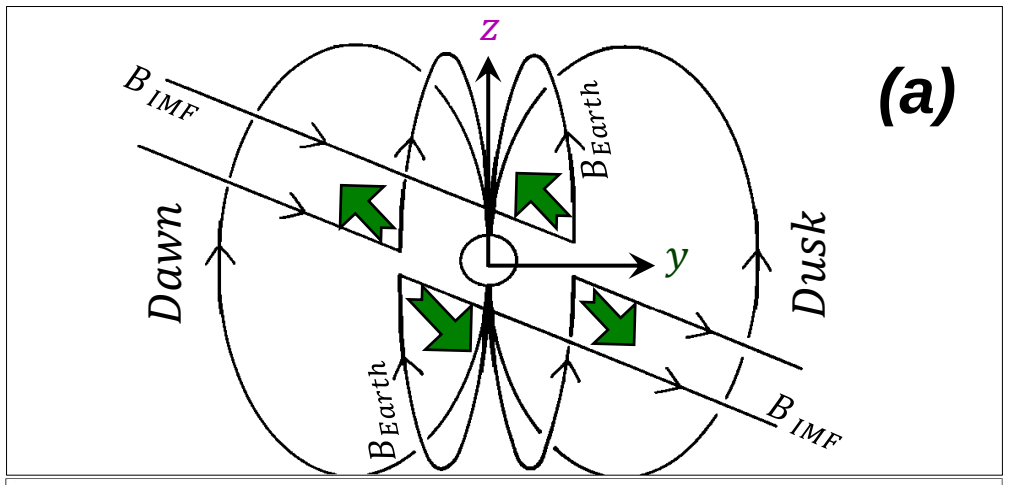

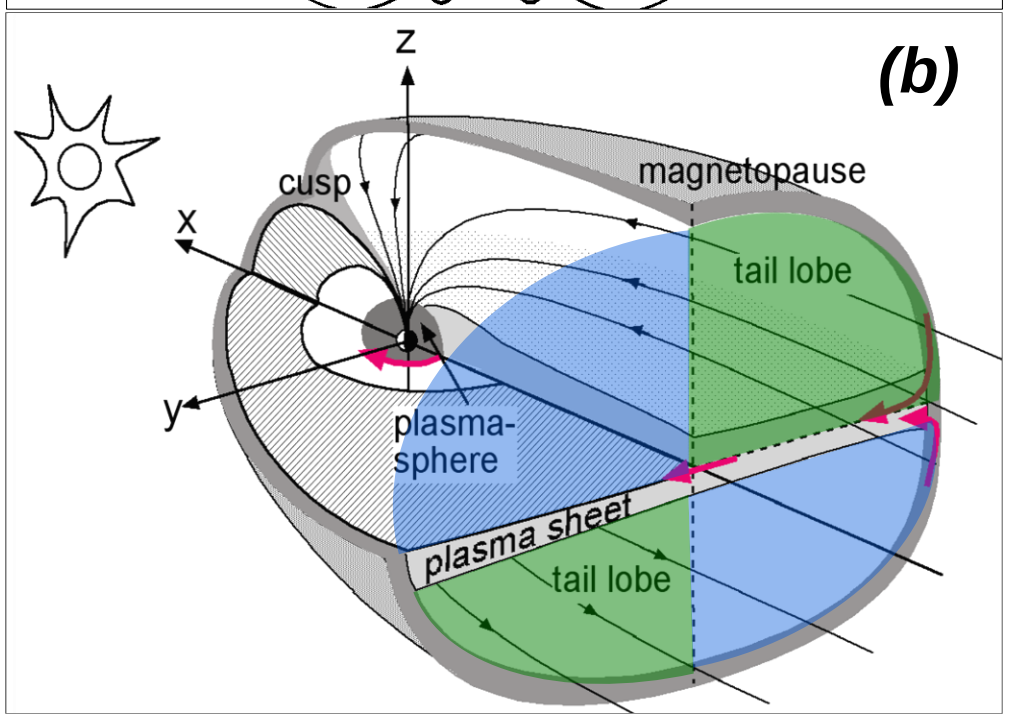

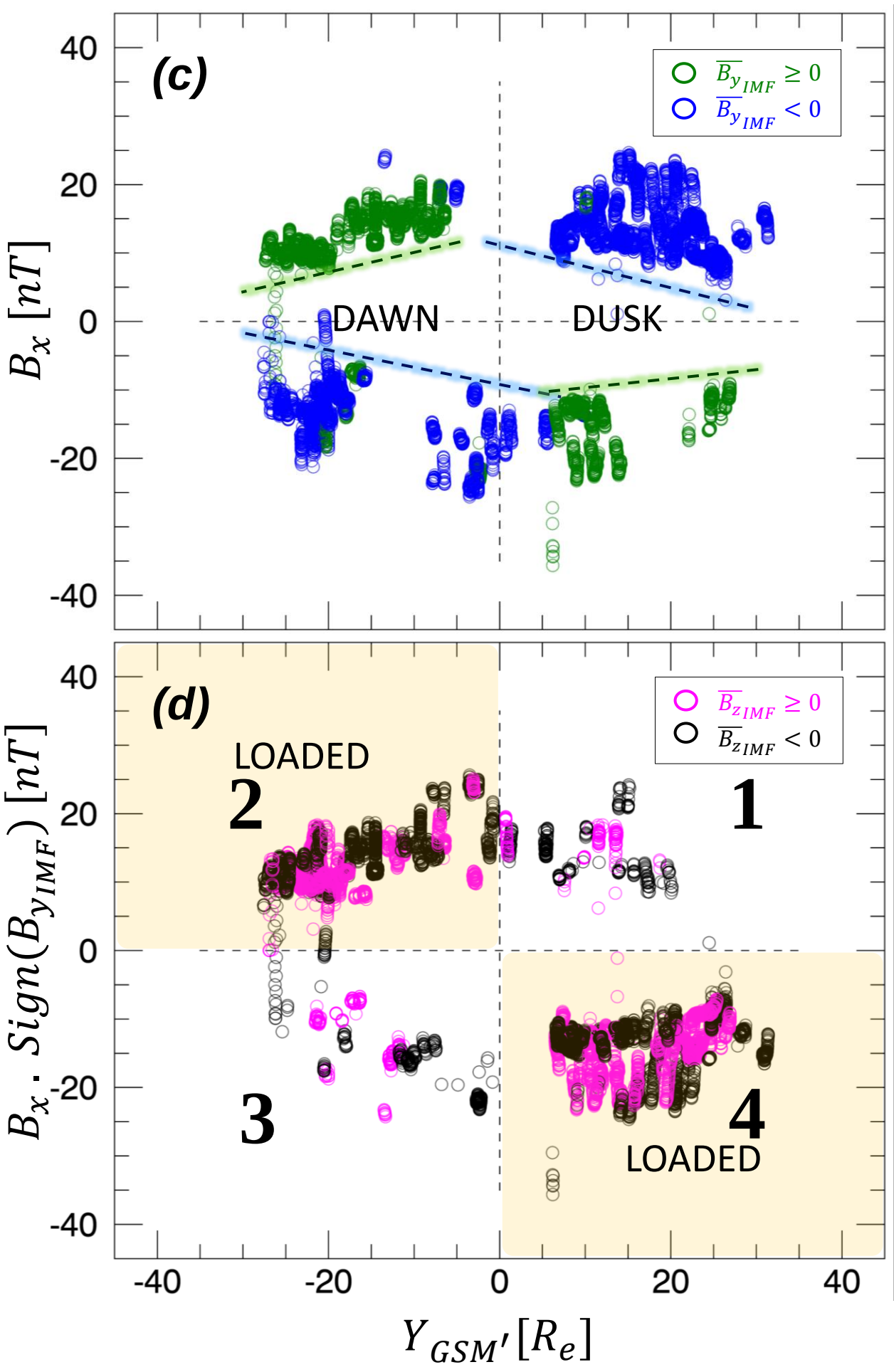

Figure 3. (a) Directions of the reconnected field lines' dragging and merging are schematically illustrated as green arrows for positive $B_{y\,IMF}$ case. (b) Expected regions of observing heavy ions in yz plane cut of magnetotail. (c) Using the same data in Figure 2, all heavy ions measurements in y (GSM' coordinate) versus the x component of magnetic field measured at magnetotail by ARTEMIS. Green circles are corresponding to the solar wind positive $B_{y\,IMF}$ and the blue circles are corresponding to the negative $B_{y\,IMF}$ on average during the even. The location of green data points are well-corelated (90% agreement) with the expected locations of measurements down the tail as depicted in panel (b) with the similar shaded colors corresponding to the same $\overline{B_{y_{IMF}}}$ orientation (green is positive and blue is negative). (d) Quadrant plot for the same data. Magenta circles are corresponding to the solar wind positive $B_{z\,IMF}$ and the black circles are corresponding to the negative $B_{z\,IMF}$. The yellow-shaded regions are loaded (number 2 and 4) quadrants. Data points (circles) in (c-d) are down-sampled to one-minute cadence. IMF data are the OMNI data. The data in (c-d) are in GSM' coordinate coordinate system which is same as GSM but rotated 4 degrees dawnward to account for the aberration due to the orbital motion of the Earth with respect to the sun. In the GSM' coordinate, the OMNI data are time shifted by 40 minutes to account for the delay between arrival of the solar wind at the location of the ARTEMIS spacecraft (the lunar orbit) and the location of the magnetopause at the dayside nose of the magnetosphere. The loaded quadrants occurrence rate is more than ~90% of the total data points. Panel (a) is adapted from Gosling et al., 1985, and panel (b) is adapted from Figure 1.2 of http://urn.fi/URN:ISBN:952-91-5949-8 courtesy of Minna Palmroth.

Figure 4.

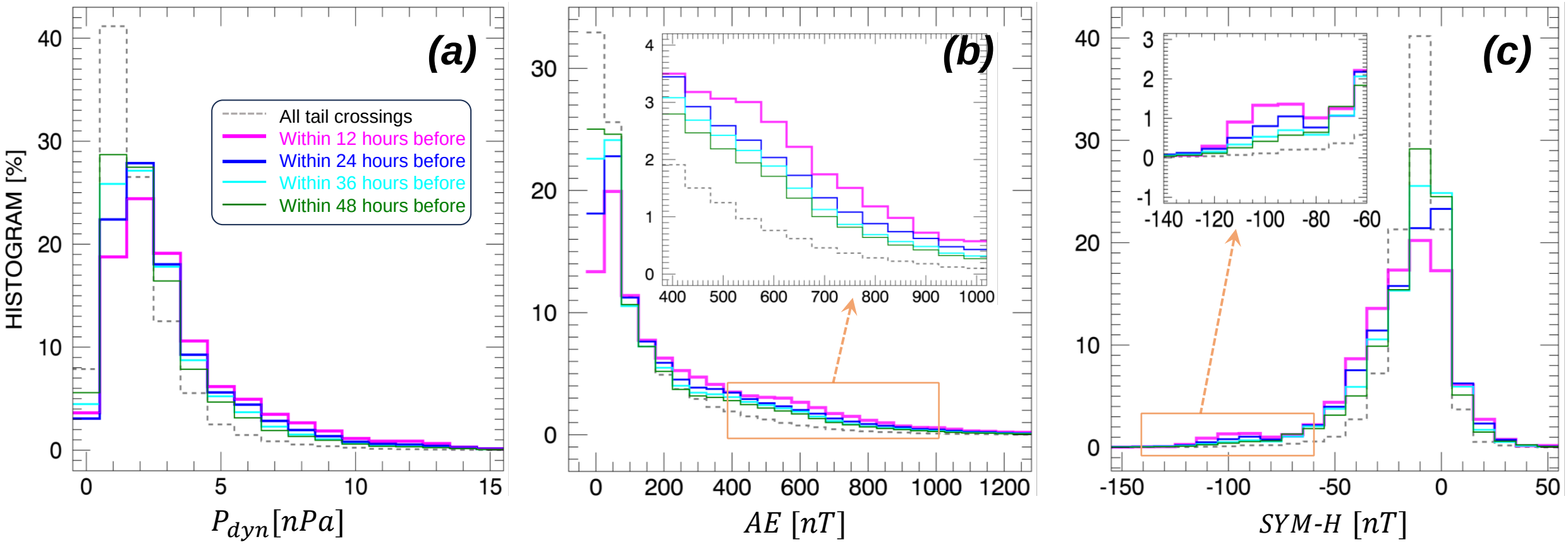

Figure 4. Histograms in % of (a) solar wind dynamic pressure, (b) Auroral Electrojet, and (c) SYM-H indices. The gray dashed lines are the occurrence during the entire times that both probes spent inside the magnetospheric tail between the two magnetopause borders (tail crossing). Magenta colors are associated with the data during the time intervals of 12 hours before until the moment the heavy ions observed at the tail. Other colors are associated with longer times until the start of observation mentioned in the legend of panel (a).

Table 1.

Index	Event Occurrence (at least once)		
$P_{dyn} > 4\ nPa$	9%	71%	1%
$AE > 800\ nT$	4%	64%	8%
$SYM - H_{min}$	20%	37%	36%
$Epoch\ Time$ $[Hours]$			

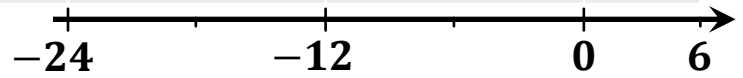

Table 1. Association of P_{dyn}, AE, and $SYM - H$ indices. The epoch time is mentioned at the bottom. Time 0 is the start time of observing COBs at the tail. The percentages are the fraction of events (among 86 events) in which the left column condition is satisfied at least once during the corresponding time interval. For example, during the 12 hours period before observing heavy ions, we see that in 71% of the events P_{dyn} was observed to be at least once above 4 nPa. The event occurrence rates do not add up to 100% since, for instance, for P_{dyn} case 19% of the events either have no associated intervals with $P_{dyn} > 4\ nPa$ periods or the P_{dyn} above $4\ nPa$ happened at longer times before the observations.

Figure 5.

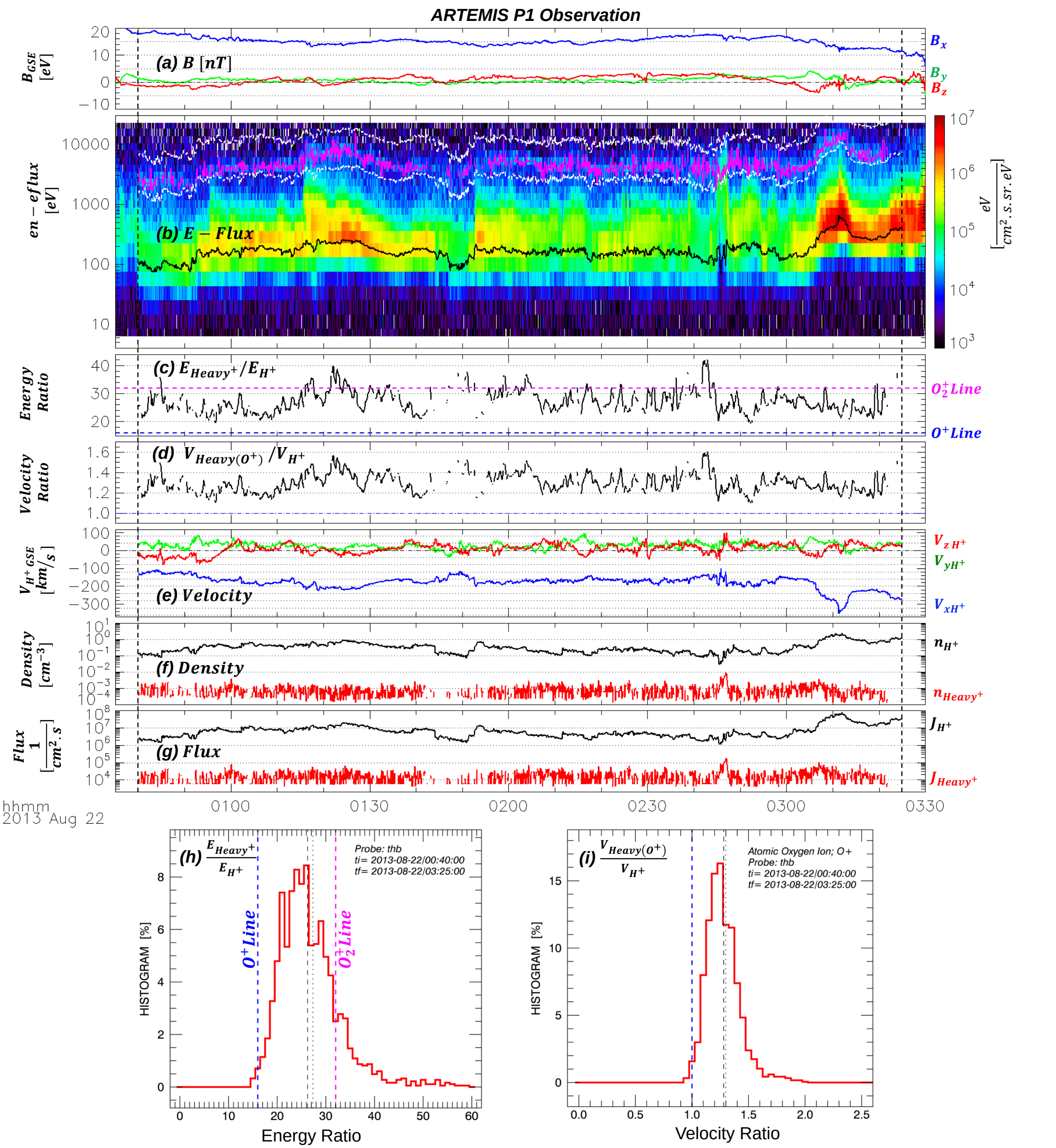

Figure 5. Magenta curve in panel (b) is E_{Heavy^+} the calculated drift energy of heavy population from the data points between the two white dashed lines while the black curve is E_{H^+} the drift energy of the proton population that calculated from the data points under the lower white dashed line. The ratio between the two calculated drift energy (running-averaged with 1 min width) is visualized in panel (c) as black curve. The blue (magenta) dashed line in (c) is the expected line if the heavy ion population contains O^+ (O_2^+) corresponding to 16 (32) assuming all species have the velocity. Panel (d) shows the calculated velocity ratio (also running-averaged with 1 min width) if the heavy ions are considered atomic oxygen O^+. Panel (e) is the proton velocities. (f) and (g) are the densities and fluxes calculated for the proton (black color) and heavy (red color) populations. (h) and (i) are histograms of the calculated energy and velocity ratios respectively. No assumption for the ions' mass is needed in (h) and no running averaging are performed for the histograms. O^+ for the heavy ions was assumed in velocity ratio calculations same as (d).

Figure 6.

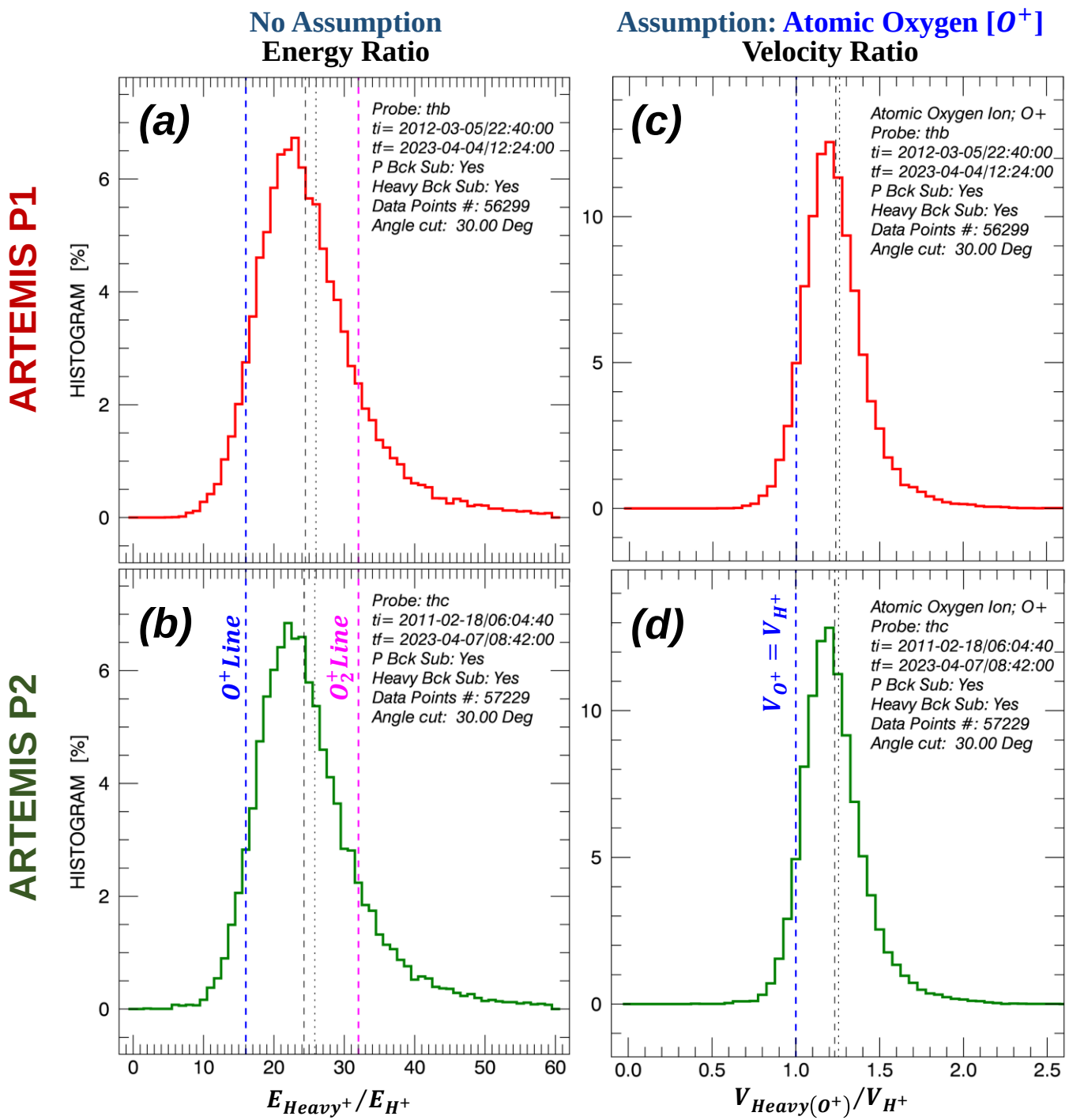

Figure 6. Histogram plots of (a) and (b) heavy ion to proton energy ratio for the entire events measured by ARTEMIS P1 (red) and ARTEMIS P2 (green) respectively, (c) and (d) atomic oxygen to proton velocity ratio for the entire events measured by ARTEMIS P1 and ARTEMIS P2 respectively. Dashed blue and dashed magenta lines in (a-b) are the expected atomic and molecular oxygen ion lines respectively if the equal-velocity assumption (with protons) is considered for the heavy ions. The dashed blue lines in (c-d) is the expected velocity if the assumed atomic oxygen ions if heavy particles happened to have exactly the same velocity as the proton population. No running average or down sampling is performed for this Figure. The locations of the measurement were already depicted in Figure 2. Dashed black and dotted black lines in all four panels are the median and mean values respectively.

Figure 7.

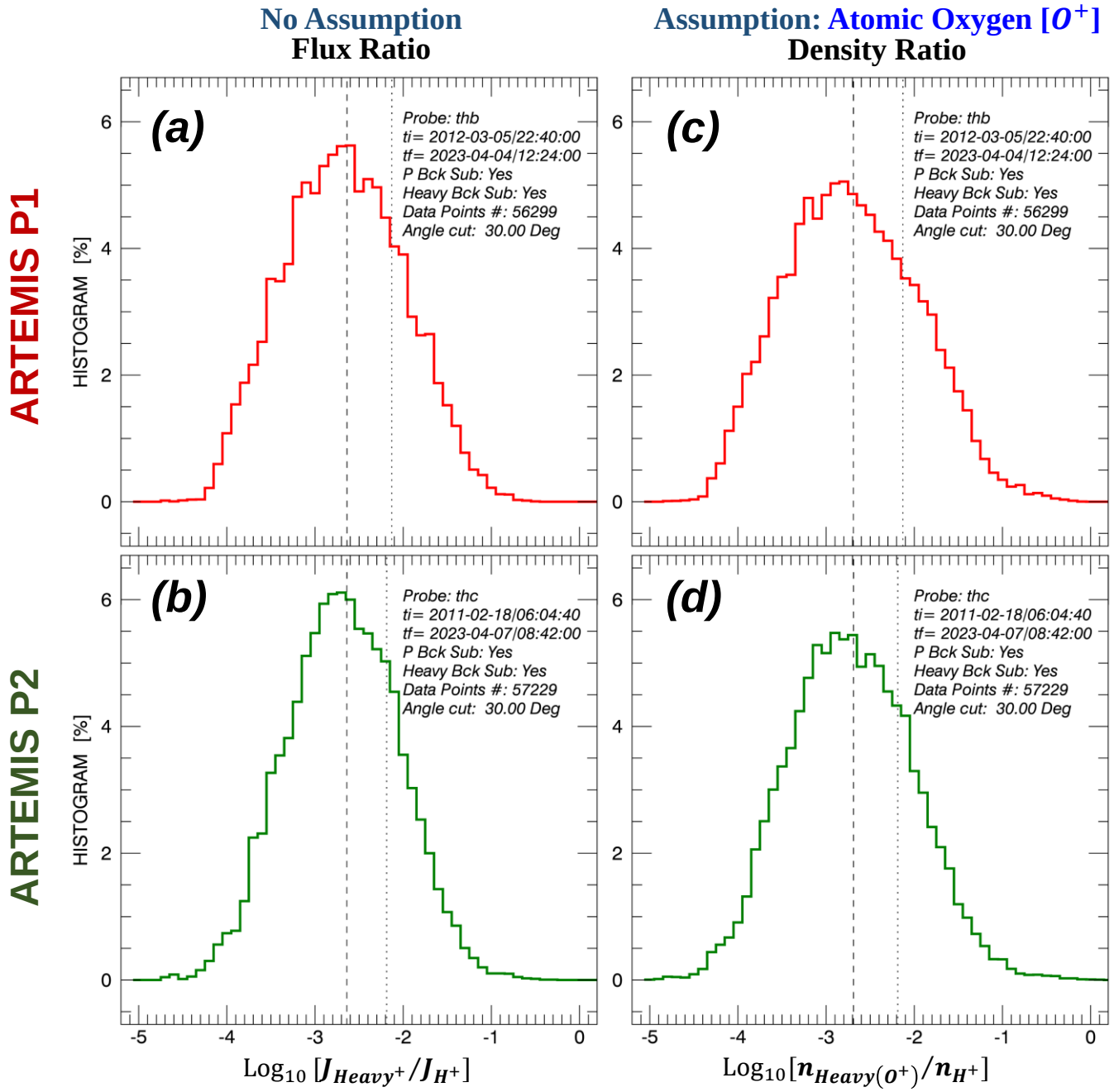

Figure 7. Histogram plots of (a) and (b) heavy ion to proton Log_{10}flux ratio for the entire events measured by ARTEMIS P1 (red) and ARTEMIS P2 (green) respectively, (c) and (d) atomic oxygen to proton Log_{10} density ratio for the entire events measured by ARTEMIS P1 (red) and ARTEMIS P2 (green) respectively. No running average or down sampling is performed for this Figure. The locations of the observation were already depicted in Figure 2. Dashed black and dotted black lines in all four panels are the median and mean values respectively.